

Distinct Diffusion in Binary Mixtures Confined in Slit Graphite Pores

C. R. Kamala

Solid State and Structural Chemistry Unit, Indian Institute of Science, 560012 Bangalore, India

K. G. Ayappa*

Department of Chemical Engineering, Indian Institute of Science, 560012 Bangalore, India

S. Yashonath

Solid State and Structural Chemistry Unit and Supercomputer Education and Research Center, Indian Institute of Science, 560012 Bangalore, India

Received: August 5, 2003; In Final Form: January 10, 2004

Distinct diffusion coefficients in the barycentric reference frame for equimolar binary mixtures confined in slit-shaped graphite pores have been evaluated using equilibrium molecular dynamics simulations. In all mixtures the ratio of the interaction energies and mass ratios are similar to those of a Xe–Ar mixture with σ_{22}/σ_{11} varied between 1 and 1.4. When $\sigma_{22}/\sigma_{11} = 1.0$ both species adsorb in similar layers in the pore and the distinct diffusion is positive. As σ_{22}/σ_{11} is increased, the distinct diffusion is found to become progressively more negative. This increasing associative tendency as σ_{22}/σ_{11} is increased is predominantly due to the formation of distinct layers by individual species. In-plane pair correlation functions also reveal the increased association between unlike species with increasing σ_{22}/σ_{11} . The Xe–Ar mixture is observed to be associative, with negative values of the distinct diffusion when the fluid forms two layers in the pore. At smaller pore widths, where only a single layer is accommodated, the mixture is weakly dissociative. Simulations with a non-Lorentz–Berthelot mixture were carried out to illustrate the effect of the interaction between unlike species.

1. Introduction

An understanding of transport properties of mixtures confined in nanoporous materials is important to processes such as gas separations, catalysis, boundary lubrication, and enhanced oil recovery. Structural and dynamic properties of fluid mixtures confined within nanopores have been widely studied using Monte Carlo and molecular dynamic (MD) simulations in a variety of nanoporous hosts such as zeolites,^{1–4} carbon nanotubes,⁵ and slit-shaped pores.^{6–9} In this chapter we study the dynamics of fluid mixtures confined in slit-shaped graphitic pores. The slit pore not only is a realistic geometry for graphite and pillared clays but also mimics the confinement geometry of the surface force apparatus that is used to correlate structure and dynamics of molecularly thin confined films.¹⁰ In addition to analyzing fluid structure, MD simulations¹¹ have been used to obtain the transport properties of individual components in confined mixtures. In this regard equilibrium MD simulations are used to calculate transport properties using appropriate Green–Kubo¹² relationships. Within the framework of equilibrium statistical mechanics, self-diffusivities can be obtained from the velocity autocorrelation function (VACF) of the confined fluid.

To completely describe the diffusive flux in a mixture, one requires a knowledge of the mutual or chemical diffusivities. In an equilibrium MD simulation, the mutual diffusivity has contributions from both VACFs and velocity cross-correlation functions (VCCF).¹³ The contribution to the mutual diffusivity from the VCCFs is known as distinct diffusivity, which can be

either negative or positive. The mutual diffusivity, D_{11} is the sum of the self-diffusivity, D_s and distinct diffusivity, D_d . Hence $D_{11} = D_s + D_d$. Positive values of the distinct diffusion coefficient can be interpreted as a tendency of the mixture to demix, whereas a negative distinct diffusion coefficient implies an associative behavior.¹⁴

The self diffusivities and mutual diffusivities for Lennard-Jones, LJ,^{13–18} and ionic mixtures¹⁹ in bulk fluids have been obtained from MD simulations. Most of the studies on binary LJ mixtures confirm that it is essential for the mixture to be highly asymmetric to show any significant contribution from the VCCFs to mutual diffusion. Studies of LJ mixtures with varying $\mu = \sigma_{22}/\sigma_{11}$ and $\nu = \epsilon_{22}/\epsilon_{11}$, show a contribution from the distinct diffusion to mutual diffusion over a certain range of μ and ν .¹⁶ Here σ_{11} , σ_{22} , ϵ_{11} , and ϵ_{22} are the LJ interaction parameters for the two components of a binary mixture. Schoen¹⁶ calculated the ratio $R = D_{11}/D_s$, which was found to be less than 1.1 for mixtures with $\nu = 1.0$ and $1.0 < \mu < 1.5$. For mixtures with $\mu = 1.0$ and $1.0 < \nu < 3.0$, R was found to have a maximum value of 1.4 for $\nu = 3.0$. In non-Lorentz–Berthelot mixtures,¹⁴ the distinct diffusion is positive, when the attraction between unlike species is weak. In contrast, for mixtures where interaction between unlike species is the strongest, the distinct diffusion is negative. As opposed to LJ mixtures, ionic mixtures show appreciable cross-correlations.¹⁹ Here the mutual diffusion is generally retarded due to the long-range attraction between the unlike ions. Recent studies on an Ar–Kr mixture show that, although individual VCCFs are nonzero, there is little contribution from distinct diffusion to the mutual diffusion.¹³ Thus an Ar–Kr mixture behaves like

* Corresponding author. E-mail: ayappa@chemeng.iisc.ernet.in.

an ideal mixture from this point of view. With the exception of a few recent studies on confined fluid mixtures,^{20,21} the literature on mutual diffusivities is largely restricted to bulk binary mixtures.

To analyze transport of mixtures through porous membranes, mutual or transport diffusivities can be obtained from a nonequilibrium simulation technique that combines grand canonical Monte Carlo and molecular dynamics simulations. In this technique a gradient in chemical potential is maintained across a porous membrane and the transport coefficient is obtained by directly computing the fluxes and forces in the system.^{22,23} Although this method mimics the experimental conditions, the simulations are elaborate and mutual diffusion coefficients obtained in this manner can have contributions from viscous flow as well.²⁴

As an alternate to nonequilibrium simulations, mutual diffusivities can be obtained from equilibrium MD simulations using the VACF and VCCFs. We have recently carried out MD simulations of equimolar Ar–Kr mixtures in zeolite NaY.²¹ At a temperature of 200 K, where the particles are strongly localized in their adsorption sites, the distinct diffusivity is negative and at 600 K it is nearly zero. Although Ar–Kr mixtures do not show any distinct diffusivity in the bulk, our study reveals that confinement can significantly alter this situation. In this manuscript we seek to improve our understanding of the effect of confinement on mutual diffusion by investigating mixtures confined to slit pores. In contrast to zeolites such as NaY, where the adsorption sites form a 3D lattice within the zeolite cavity, adsorption sites in a slit pore lie in a plane parallel to the pore walls. Hence the fluid adsorbs in layers leading to an inhomogeneous fluid. This layering is likely to influence the dynamic correlations between like and unlike species and hence affect the mutual diffusivities of the confined fluid.

We carry out microcanonical (NVE) MD simulations for a binary mixture of monatomic particles that interact via a Lennard-Jones potential. The fluid is confined in a smooth slit graphite pore where the interaction between a fluid atom and the wall is only a function of the normal distance of the fluid particle from the wall. Mutual diffusivities are evaluated in the barycentric reference frame for four different binary mixtures with different size ratios, keeping their mass and energy ratios fixed. One of these correspond to a Ar–Xe mixture with the other mixtures having similar energy and mass ratios as the Ar–Xe mixture. The changes in size ratios influences the separation between density distributions of each species in the mixture. Simulations are carried out at a pore width where the fluid forms two well-resolved layers for each species. In addition to computing the VACFs and VCCFs, the in-plane pair correlation functions are also evaluated.

2. Theory

2.1. Mutual Diffusivity. Within the framework of equilibrium statistical mechanics the mutual diffusivity in a mixture can be computed from a knowledge of two time correlation functions of the mixture. The first of these is the VACF,

$$C_a^\alpha(t) = \langle v_i(\tau) \cdot v_i(\tau+t) \rangle_{\tau, N_\alpha} \\ = \frac{1}{3N_\alpha} \sum_{i=1}^{N_\alpha} \langle v_i(t+\tau) \cdot v_i(t) \rangle_\tau \quad \alpha = 1, 2 \quad (1)$$

where $v_i(t)$ is the velocity of i th particle of α th species and the subscript τ represents averaging over shifted time origins from

velocities generated during a molecular dynamics simulation. The second time correlation function is the VCCF,

$$C_c^{\alpha\beta}(t) = \langle v_i(\tau) \cdot v_j(\tau+t) \rangle_{\tau, N} \\ = \frac{1}{3N} \sum_{i=1}^{N_\alpha} \sum_{j=1}^{N_\beta} \langle v_i(t+\tau) \cdot v_j(t) \rangle_\tau \quad \text{when } \alpha, \beta = 1, 2 \text{ and } \alpha \neq \beta \\ = \frac{1}{3N} \sum_{i=1}^{N_\alpha} \sum_{j \neq i}^{N_\alpha} \langle v_i(t+\tau) \cdot v_j(t) \rangle_\tau \quad \text{when } \alpha = 1, 2 \text{ and } \alpha = \beta \quad (2)$$

where $N = N_1 + N_2$ is the total number of particles in the system. All time correlations reported in this manuscript are computed in the center of mass or barycentric reference frame where the reference velocity is

$$v^M = \frac{\sum_{i=1}^N m_i v_i}{\sum_{i=1}^N m_i} \quad (3)$$

The implications of the appropriate choice of reference frames while computing mutual diffusivities for confined mixtures has been elucidated in our earlier molecular dynamics study.²¹

The Green–Kubo relations for the mutual diffusivity^{13,25,26} in a binary mixture consisting of N_1 particles of species one and N_2 particles of species two is given by

$$D_{11} = Q \left(x_2 D_1 + x_1 D_2 + x_1 x_2 \left[\frac{f_{11}}{x_1^2} + \frac{f_{22}}{x_2^2} - 2 \frac{f_{12}}{x_1 x_2} \right] \right) \quad (4)$$

The above expression for the mutual diffusivity can be grouped into two main contributions. The first contribution is

$$D_s = Q(x_2 D_1 + x_1 D_2) \quad (5)$$

where Q is the thermodynamic factor and x_1 and x_2 are the mole fractions of species one and two, respectively. In eq 5 the contributions to D_s arise solely from the self-diffusivities, which are related to the VACF.

$$D_\alpha = \int_0^\infty C_a^\alpha(t) dt \quad \alpha = 1, 2 \quad (6)$$

The second contribution is from the distinct diffusion, D_d , which depends only on the VCCFs,

$$D_d = Q \left(x_1 x_2 \left[\frac{f_{11}}{x_1^2} + \frac{f_{22}}{x_2^2} - 2 \frac{f_{12}}{x_1 x_2} \right] \right) \quad (7)$$

where

$$f_{\alpha\beta} = \int_0^\infty C_c^{\alpha\beta}(t) dt \quad \alpha, \beta = 1, 2 \quad (8)$$

In the above equations, the thermodynamic factor

$$Q = [1 + x_1 x_2 \rho (\Gamma_{11} + \Gamma_{22} - 2\Gamma_{12})]^{-1} \quad (9)$$

where Γ_{ij} is related to the radial distribution function g_{ij} by

$$\Gamma_{\alpha\beta} = 4\pi \int_0^\infty r^2 [g_{\alpha\beta}(r) - 1] dr \quad \alpha, \beta = 1, 2 \quad (10)$$

Equation 4 is used for the calculation of mutual diffusivities in this work. The ratio R , $R = \mathcal{D}_{11}/\mathcal{D}_s$, which is a measure of dynamic dissociation ($R > 1$) and association ($R < 1$) of the mixture is also a measure of the relative importance of the cross-correlations on the mutual diffusion and hence a measure of the deviation from an ideal mixture ($R = 1$). In this manuscript we report the quantities,

$$\mathcal{D}_s = D_s/Q \quad \text{and} \quad \mathcal{D}_d = D_d/Q \quad (11)$$

Hence $\mathcal{D}_{11} = \mathcal{D}_s + \mathcal{D}_d$. It has been shown previously that the VCCFs can be expressed in terms of VACFs.²¹ Hence

$$C_c^{\alpha\beta}(t) = C_s^{\alpha\beta}(t) - x_\alpha C_a^{\alpha}(t) \delta_{\alpha\beta} \quad \alpha, \beta = 1, 2 \quad (12)$$

where $\delta_{\alpha\beta}$ is the Kronecker delta and

$$C_s^{\alpha\beta}(t) = \frac{1}{3N} \langle \mathbf{S}_\alpha(\tau) \cdot \mathbf{S}_\beta(\tau+t) \rangle_\tau \quad (13)$$

is the correlation between the sum of the velocities of individual species where

$$\mathbf{S}_\alpha(\tau) = \sum_{i=1}^{N_\alpha} \mathbf{v}_i(\tau) \quad \alpha = 1, 2 \quad (14)$$

Equations 12 are used to compute the cross-correlations because they reduce the computational effort from order N^2 to order N when $\alpha \neq \beta$ and order 1 when $\alpha = \beta$.

Because the fluid is confined in a slit pore, as shown in Figure 1, we are interested only in the dynamics in the direction parallel to the wall. In this case only the x and y (in-plane) components of the particle velocities are used for computing the time correlation functions, the factor 3 in eqs 1, 2, and 13 is replaced with a factor of 2.

2.2. Structural Properties. The layer density distribution, $\rho(z)$ gives the density distribution of particles in a direction normal to the pore walls.

$$\rho_\alpha(z) = \left\langle \frac{N_\alpha(z - \Delta z/2, z + \Delta z/2)}{A \Delta z} \right\rangle \quad (15)$$

where A is the area of the slit pore and N_α is the number of particles of the α th species located in a bin of width Δz around z .

The in-plane radial distribution function

$$g_{\alpha\beta}^{xy}(r) = \left\langle \frac{N_\beta(r - \Delta r/r, r + \Delta r/r)}{2\pi r \Delta r \Delta z \rho_{\alpha\beta}} \right\rangle \quad (16)$$

where $\rho_{\alpha\beta} = (\rho_\alpha + \rho_\beta)/2A\Delta z$ is the layer density. Because all the radial distributions reported in this work are in the x - y plane, the superscript in the above equation will henceforth be dropped.

3. Interaction Potential

The interaction between the adsorbed fluid atoms are modeled using the (6-12) Lennard-Jones (LJ) potential.

$$U(r_{ij}) = 4\epsilon[(\sigma/r_{ij})^{12} - (\sigma/r_{ij})^6] \quad (17)$$

where σ is the diameter of the particle and ϵ is the interaction

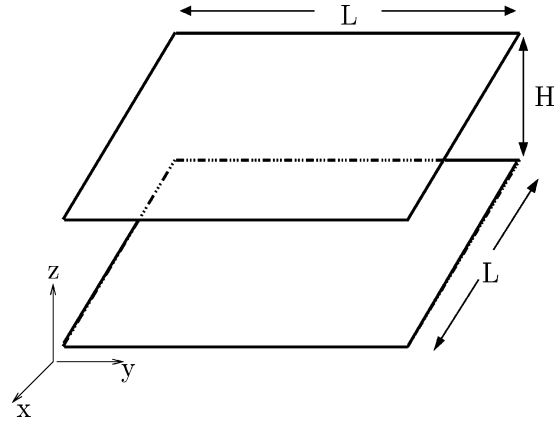


Figure 1. Schematic of a graphite slit pore consisting of two graphite layers of length L in x and y directions. The two sheets are separated by distance H along the z axis, which is the pore width.

strength. The potential parameters for unlike species are obtained using Lorentz–Berthelot (LB) combination rules unless stated otherwise.

The confining medium is characterized by two graphite walls separated by a distance H along the z direction as shown in Figure 1. The interaction potential between a fluid atom and a single graphite sheet is given by the 10-4-3 potential²⁷

$$\phi_{fw}(z) = 2\pi\rho_w\epsilon_{fw}\sigma_{fw}^2\Delta\left[\frac{2}{5}\left(\frac{\sigma_{fw}}{z}\right)^{10} - \left(\frac{\sigma_{fw}}{z}\right)^4 - \left(\frac{\sigma_{fw}^4}{3\Delta(z + 0.61\Delta)^3}\right)\right] \quad (18)$$

where the subscript f and w represent fluid and wall, respectively, ρ_w is the density of carbon atoms in a single graphite sheet and Δ is the spacing between the carbon sheets in graphite.

The parameters for graphite wall²⁷ are

$$\begin{aligned} \sigma_{ww} &= 3.40 \text{ \AA} & \epsilon_{ww} &= 0.2327 \text{ kJ/mol} \\ \rho_w &= 0.114 \text{ \AA}^{-3} & \Delta &= 3.35 \text{ \AA} \end{aligned}$$

The third term in eq 18 represents an attractive contribution from the layers beyond the first layer and is an order of magnitude smaller than the first two terms. To evaluate the importance of this term on the dynamics, VACFs were computed and the self-diffusion coefficients were evaluated for the mixture M4 (see Table 1) for the full 10-4-3 potential given in eq 18

TABLE 1: Lennard-Jones Parameters for the Fluid–Fluid Interactions

system	σ_{11}	σ_{22}	ϵ_{11}	ϵ_{22}
M1	3.405	3.405	1.0	1.83
M2	3.405	4.1	1.0	1.83
M3	3.405	4.4	1.0	1.83
M4	3.405	4.767	1.0	1.83

and the 10-4 potential obtained by neglecting the third term. Because the VACFs were found to be identical, the third term was neglected and only the 10-4 part of the potential was considered for all our simulations. For a given pore with the two walls separated by a width H , the total potential energy from both the walls, one located at $z = 0$ and the other located at $z = H$ is given by

$$U_{fw}(z) = \phi_{fw}(z) + \phi_{fw}(H - z) \quad (19)$$

Simulations are carried out for four types of equimolar confined binary mixtures, whose LJ parameters are given in

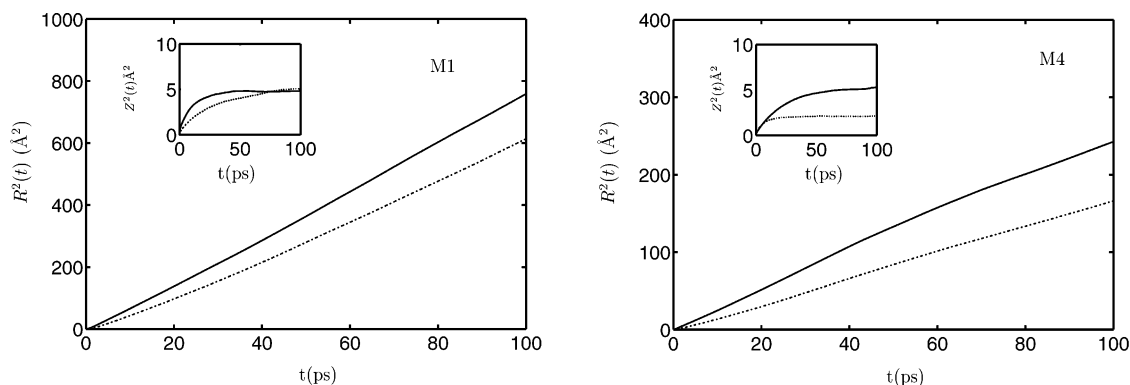


Figure 2. Mean square displacement plots for species 1 (solid line) and species 2 (dash dot) for systems M1 and M4. The inset showing the mean square displacement along the z direction illustrates the nondiffusive behavior in this direction.

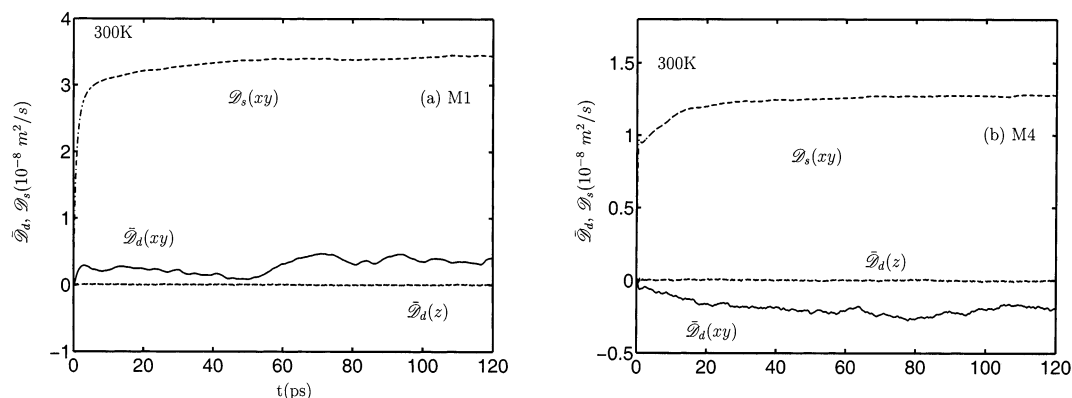


Figure 3. Distinct and mixture self-diffusivities for systems M1 (a) and M4 (b). It is seen that the distinct diffusion ($\bar{\mathcal{D}}_d$) is zero along the z direction. All the values for diffusion coefficients reported are in the xy plane. $\bar{\mathcal{D}}_d$ represent data averaged over 12 MD runs.

Table 1. The parameters for system M2 correspond to a Xe–Ar mixture. Mixtures M1, M3, and M4 represent mixtures that have similar LJ energies as mixture M2; however, the LJ diameter for species 2 is changed. Hence the ratios $\epsilon_{22}/\epsilon_{11}$ for all the mixtures are identical and only the ratios σ_{22}/σ_{11} are varied. The atomic masses for the individual components for all the mixtures correspond to those of argon ($m_1 = 40$ amu) and xenon ($m_2 = 131$ amu). In addition, simulations for one non-LB mixture was also carried out with $\epsilon_{12} = 0.6$ kJ/mol and all other parameters were similar to those of mixture M4. The value of ϵ_{12} for the non-LB mixture is lower when compared to $\epsilon_{12} = 1.3527$ kJ/mol, for the corresponding LB mixture.

4. Simulation Details

All simulations have been carried out in the microcanonical ensemble (NVE) with periodic boundary conditions along the x and y directions (Figure 1). The number of fluid particles was 400 (200 particles of each species), which corresponds to a number density of $5.72475 \times 10^{-3} \text{ \AA}^{-3}$. Unless stated otherwise, a pore of width $H = 10.43 \text{ \AA}$ and a simulation cell of length 81.848 \AA along the x and y directions was used in all the simulations. A potential cutoff distance of 14.446 \AA is used, which corresponds to 3.03 times the LJ diameter of the largest species studied ($\sigma_{22} = 4.767 \text{ \AA}$). The properties were accumulated for 1.5 ns after an equilibration period of 500 ps with a time step of 10 fs. The integration was carried out using the velocity Verlet algorithm.²⁸ The collective properties, i.e., VCCFs and the distinct diffusivities were averaged over 12 such 1.5 ns runs for better statistics. The positions and velocities were stored every 20 fs for the calculation of properties of interest. The temperature of the system was maintained at 300 K for all the runs carried out.

5. Results and Discussion

5.1. Mean Squared Displacements and Density Distributions. Prior to presenting results for the VCCFs and the distinct diffusion, the contributions to the self- and distinct diffusion from in-plane (x – y) and out-of-plane (z) directions are investigated. Because the system is finite in the z -direction, the pore fluid is not expected to be diffusive in this direction.²⁹ To verify this, the mean square displacements in x , y , and z directions for mixture M1 and M4 (Figure 2) were computed using

$$\langle R^2(t) \rangle = \langle |\mathbf{r}(t) - \mathbf{r}(0)|^2 \rangle \quad (20)$$

where $\mathbf{r}(t) = \bar{e}_x x(t) + \bar{e}_y y(t) + \bar{e}_z z(t)$, and

$$\langle Z^2(t) \rangle = \langle |z(t) - z(0)|^2 \rangle \quad (21)$$

The angular brackets indicate averages over all particles and time origins. In both cases the absence of a linear regime in the z -direction clearly indicates the absence of a diffusive motion along this direction. In contrast, the linear MSD along the xy directions indicates that the motion is diffusive. Hence the self-diffusivities are reported only in the xy plane. Figure 3 illustrates both the xy and z contributions to the distinct diffusion \mathcal{D}_d (eq 7) for M1 and M4 as a function of time. The distinct diffusivity data represent averages over 12 independent MD simulations. The in-plane mixture self-diffusivity, $\mathcal{D}_s(xy)$ is shown as well. In both mixtures the contributions to the distinct diffusion along the z direction is absent. In what follows, the reported \mathcal{D}_s and \mathcal{D}_d represent contributions from motion in the xy plane only.

Figure 4 illustrates the layer density distributions for the four mixtures investigated. The pore width H and the fluid density are such that a given species can form two distinct fluid layers.

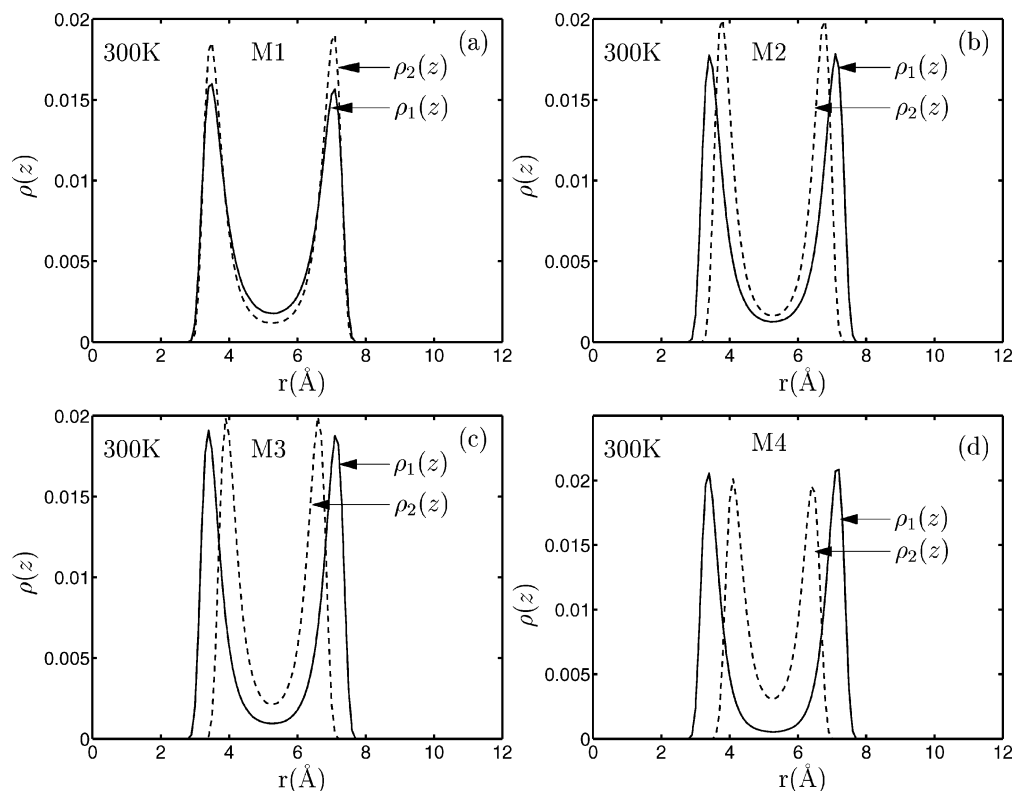


Figure 4. Density distribution of particles along the z direction in the slitpore. The solid line is the distribution for species 1 and the dashed line is for species 2. Mixtures: (a) M1; (b) M2; (c) M3; (d) M4. As the ratio of the molecular diameters is increased from M1 to M4, increased segregation is observed between the fluid layers. In mixture M1 where both species have similar diameters they occupy the same layer within the pore.

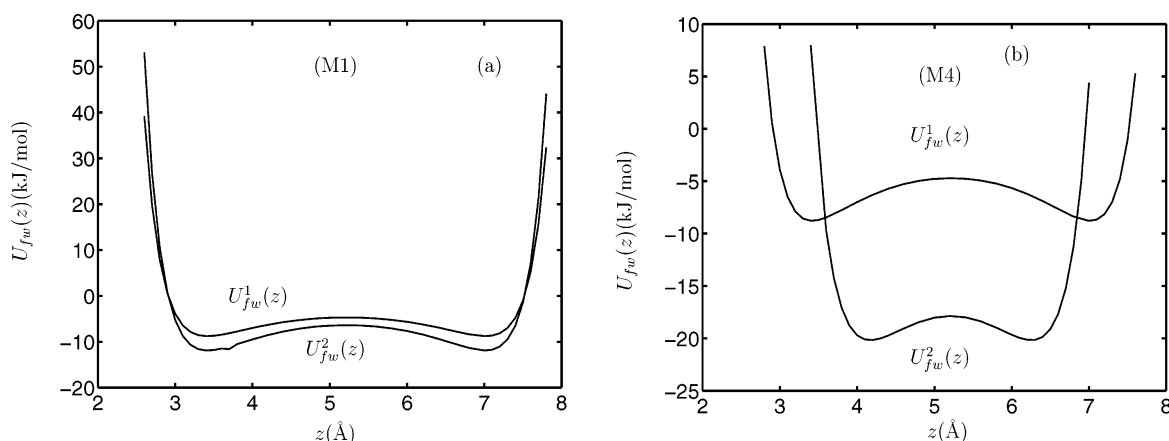


Figure 5. Potential energy surface of species 1 and 2 in graphite slit pore. Species 2 has a deeper potential well compared to species 1 and is more toward the center of the pore.

For the mixture M1 ($\sigma_{22}/\sigma_{11} = 1$) both particles compete for the similar z location in the pore leading to overlapping density distributions, as seen in Figure 4a. As the ratio σ_{22}/σ_{11} is increased, from mixture M1 to M4, the density peak corresponding to species 2 in the mixture shift away from the wall, toward the central regions of the pore. System M4 (Figure 4d, $\sigma_{22}/\sigma_{11} = 1.4$) illustrates the least amount of overlap between density distributions and represents the mixture where segregation between different species is the greatest. Differences in density distributions are largely due to changes in the location of the fluid–wall potential energy minima as the ratio σ_{22}/σ_{11} is varied. Figure 5a,b illustrates the fluid–wall potential for M1 and M4, respectively. In addition to shifting the position of the density distribution for different species, altering σ_{22}/σ_{11} increases the depth of the interaction potential for the larger species, as seen in Figure 5b.

5.2. Distinct Diffusivity and VCCFs. Figure 6 illustrates the distinct diffusion coefficients as a function of time obtained by evaluating

$$\mathcal{D}_d(t) \equiv D_d/Q = \left(x_1 x_2 \left[\frac{f_{11}(t)}{x_1^2} + \frac{f_{22}(t)}{x_2^2} - 2 \frac{f_{12}(t)}{x_1 x_2} \right] \right) \quad (22)$$

where

$$f_{\alpha\beta}(t) = \int_0^t C_c^{\alpha\beta}(\tau) d\tau \quad \alpha, \beta = 1, 2 \quad (23)$$

The dashed lines represent \mathcal{D}_d calculated from individual runs and the solid lines represent the average value, $\bar{\mathcal{D}}_d$, averaged over 12 runs. Because \mathcal{D}_d are obtained as time integrals of the VCCFs (eq 23), they start from the origin at zero time. The

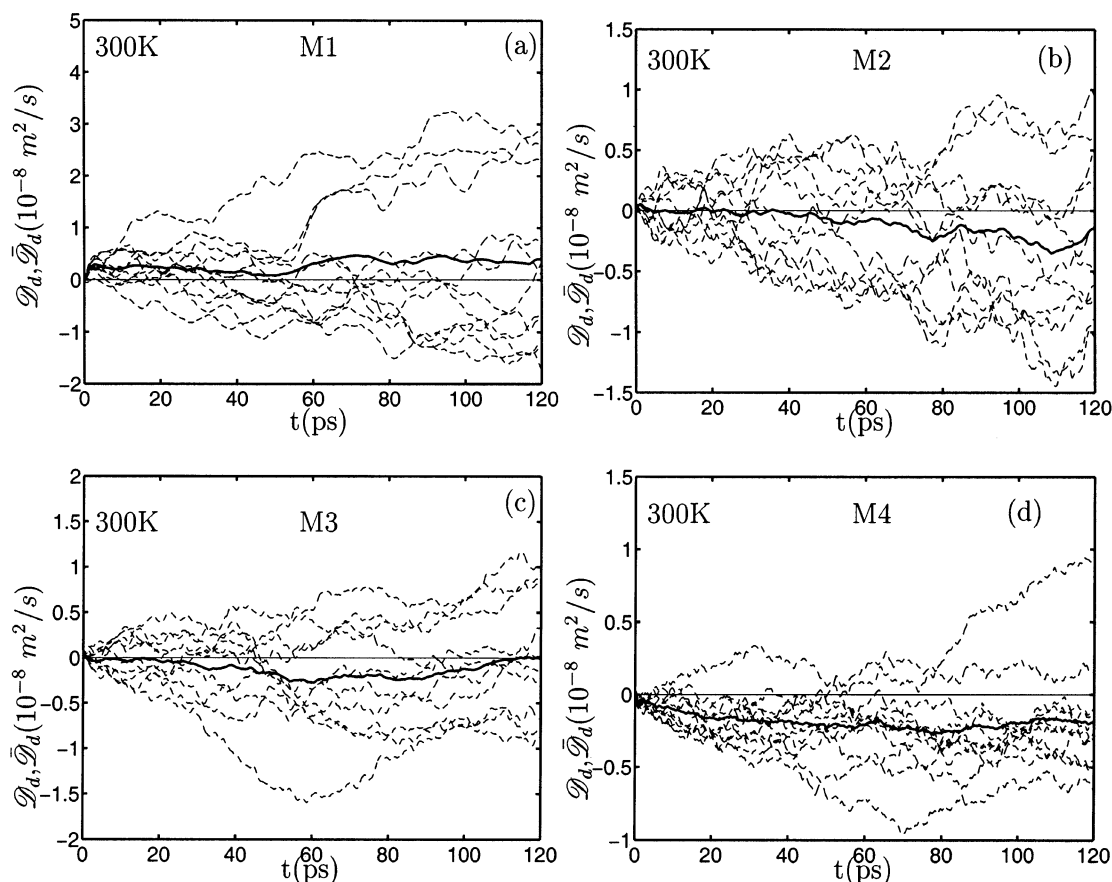


Figure 6. Distinct diffusion coefficients in (a) M1, (b) M2, (c) M3, and (d) M4, calculated from single runs (\mathcal{D}_d , dotted lines) and averaged over 12 simulation runs ($\bar{\mathcal{D}}_d$, solid line). In all cases averaging is seen to greatly reduce the uncertainties associated with the distinct diffusivity. The distinct diffusion, \mathcal{D}_d is positive only for mixture M1.

large uncertainties associated with computing the distinct diffusivity D_d are reflected in Figure 6. The source of these uncertainties lies in the VCCFs, which are collective properties representative of the entire system. In contrast, the VACFs are single particle properties and benefit from averaging over N particles in the system. As a consequence VCCFs show larger fluctuations when compared with the VACFs. These large uncertainties in transport properties computed from VCCFs have also been observed in other molecular dynamic simulations of mixtures in zeolites.^{21,20} To reduce uncertainties in the transport diffusivity, averages are obtained over a sufficiently large number of independent MD simulations. Averaging is seen to greatly reduce the fluctuations in \mathcal{D}_d (Figure 6) and $\bar{\mathcal{D}}_d$ is seen to approach a steady value by approximately 60 ps.

As a further evaluation of the uncertainties in \mathcal{D}_d we compute

$$\langle \bar{\mathcal{D}}_d \rangle = \frac{1}{t_2 - t_1} \sum_{t=t_1}^{t_2} \bar{\mathcal{D}}_d(t) \quad (24)$$

which represents the average of $\bar{\mathcal{D}}_d(t)$ for $t_1 < t < t_2$. We note that the transport diffusivity \mathcal{D}_d is the long time limit ($t \rightarrow \infty$) of $\mathcal{D}_d(t)$. However, given the uncertainties in \mathcal{D}_d , computing \mathcal{D}_d by the averaging procedure in eq 24 along with its corresponding standard deviation, is expected to provide a more reliable estimate of the transport diffusivity. $\langle \bar{\mathcal{D}}_d \rangle$ evaluated using eq 24 with $t_2 = 120$ ps, as a function of t_1 is illustrated in Figure 7a along with the standard deviation over the same interval (t_1, t_2). For all mixtures, the variation in $\langle \bar{\mathcal{D}}_d \rangle$ with t_1 shown in Figure 7a is within the error bars associated with $\langle \bar{\mathcal{D}}_d \rangle$ itself. We emphasize that despite the reasonable variation

in $\bar{\mathcal{D}}_d$ with t , the overall estimates for the four mixtures are reliable and one can conclude that the data are positive for M1 and negative for the others. The values of $\langle \bar{\mathcal{D}}_d \rangle$ and its standard deviation are reported in Table 2 for $t_1 = 60$ ps. Given the large uncertainties the ordering of $\langle \bar{\mathcal{D}}_d \rangle$ values for mixtures M2 and M3 are unclear. However, the data for M4 and its relatively small variance (Figure 7) suggest that this mixture has the lowest value of \mathcal{D}_d among the mixtures studied. Figure 7b illustrates the ratio $R = \mathcal{D}_{11}/\mathcal{D}_s$ evaluated for the corresponding values of $\langle \bar{\mathcal{D}}_d \rangle$ shown in Figure 7a. The value of R is greater than unity for mixture M1 and is less than unity for mixtures M2, M3, and M4. The value of R is the least in mixture M4, implying that this mixture has the strongest association when compared to the other mixtures investigated. Given the large uncertainties in M2 and M3, it not possible to conclusively differentiate between their R values shown in Table 2.

Previous studies in bulk LJ mixtures reveal that the ratio R is a measure of dynamic dissociation and association¹⁴ in a mixture. The ratio R had values less than unity in those mixtures modeled with a higher interaction strength between particles of unlike species (ϵ_{12}) than that given by the LB mixing rule. In mixtures where ϵ_{12} is weaker than ϵ_{11} and ϵ_{22} , the ratio R was found to be greater than unity. Hence, $R > 1$ indicates a tendency of the mixture to demix or dissociate, with a tendency to mix or associate when $R < 1$. On the basis of the interaction parameters used for the various mixtures investigated, we briefly discuss the expected values of R for the corresponding bulk mixtures and the deviations therein of the mixtures observed under confinement. From previous bulk studies with binary LJ mixtures,¹⁴ mixture M1 is expected to be the most associative,

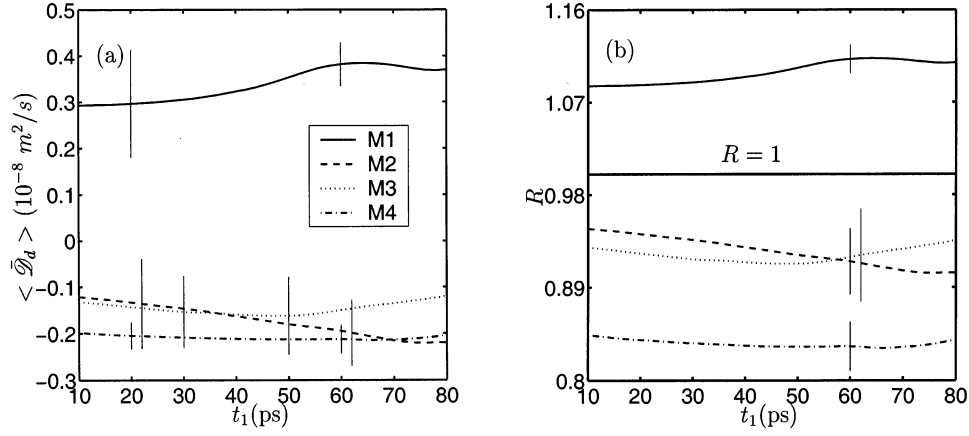


Figure 7. (a) Averaged distinct diffusivity as a function of different initial times t_1 computed using eq 24 with $t_2 = 120$ ps. Error bars shown for mixtures M1 and M4 at $t_1 = 20$ and 60 ps, for M3 at 30 and 50 ps, and M2 at 22 and 62 ps, respectively. (b) Corresponding values of $R = \mathcal{D}_{11}/\mathcal{D}_s$ as a function of t_1 with error bars at M1, M2, and M4 at $t_1 = 60$ ps and at $t_1 = 62$ ps for M3.

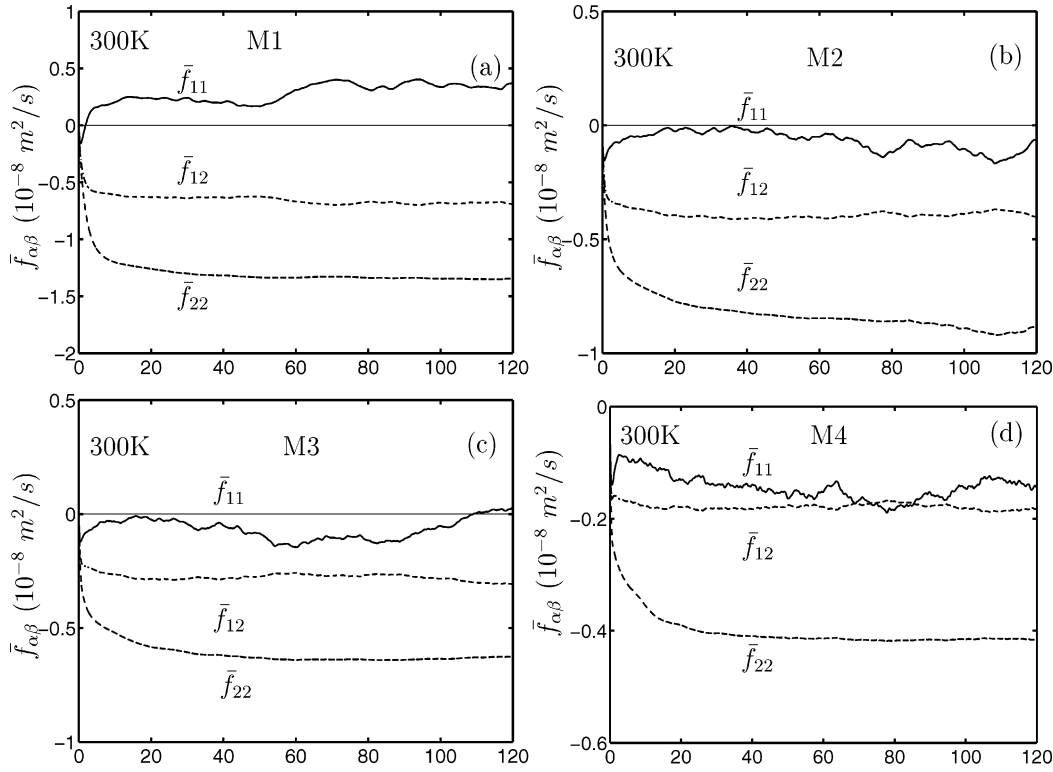


Figure 8. $\bar{f}_{\alpha\beta}$ s (running integrals of VCCFs) for mixtures (a) M1, (b) M2, (c) M3, and (d) M4. The results represent averages over 12 independent molecular dynamic simulations. The x-axis units represent time in ps.

TABLE 2: Self-Diffusivities (D_1 , D_2 and \mathcal{D}_s), Distinct Diffusivities ($\langle \bar{\mathcal{D}}_d \rangle$), and Mutual Diffusivities (\mathcal{D}_{11}) in $10^{-8} \text{ m}^2/\text{s}^a$

system	σ_{22}/σ_{11}	D_1	D_2	\mathcal{D}_s	$\langle \bar{\mathcal{D}}_d \rangle$	$\sigma_{\langle \bar{\mathcal{D}}_d \rangle}$	$R = \mathcal{D}_{11}/\mathcal{D}_s$
M1	1.0	3.815	3.007	3.411	0.382	0.047	1.112
M2	1.2	2.719	1.867	2.293	-0.195	0.073	0.915
M3	1.29	2.210	1.509	1.860	-0.150	0.084	0.919
M4	1.4	1.566	0.977	1.271	-0.212	0.031	0.833

^a $\langle \bar{\mathcal{D}}_d \rangle$ is computed from eq 24 with $t_1 = 60$ ps and $t_2 = 120$ ps.

because $\epsilon_{12}/\epsilon_{11} = 1.3527$ and $\sigma_{12}/\sigma_{11} = 1.0$. As the ratio σ_{22}/σ_{11} is increased keeping $\epsilon_{22}/\epsilon_{11}$ fixed, the mixtures should become progressively more dissociative. However, the trends observed under confinement in the slit pore are in contrast to those expected for a bulk fluid. Mixture M1 is dissociative, with progressively increased association observed on going from mixtures M2 to M4. Hence \mathcal{D}_d is positive for mixture M1 becoming more negative as the size ratios are increased from

TABLE 3: $\langle \bar{f}_{\alpha\beta} \rangle$ in $10^{-8} \text{ m}^2/\text{s}$ Evaluated Using Eq 24, with $t_1 = 60$ ps and $t_2 = 120$ ps

system	$\langle \bar{f}_{11} \rangle$	$\langle \bar{f}_{22} \rangle$	$\langle \bar{f}_{12} \rangle$	$ \langle \bar{f}_{11} \rangle + \langle \bar{f}_{22} \rangle $	$ 2.0\langle \bar{f}_{12} \rangle $
M1	0.354	-1.3390	-0.6835	0.9854	1.3671
M2	-0.0983	-0.8758	-0.3897	0.9741	0.7794
M3	-0.0724	-0.6355	-0.2789	0.7079	0.5578
M4	-0.1540	-0.4156	-0.1786	0.5697	0.3571

M2 to M4. The reasons for these deviations from bulk behavior will be discussed later in the text.

We next discuss the trends in the VCCFs that are used to compute distinct diffusivities. The running integrals of VCCFs (eq 8), f_{11} , f_{22} , and f_{12} , are shown in Figure 8 for all the four mixtures investigated. The results were obtained after averaging over 12 independent MD simulations. The average values $\langle \bar{f}_{\alpha\beta} \rangle$ as a function of t_1 are obtained in a similar manner as \mathcal{D}_d (eq 24). The values of $\langle \bar{f}_{ij} \rangle$ obtained for $t_1 = 60$ ps are tabulated in Table 3. For the mixture M1 (Figure 8a), f_{11} is negative at initial

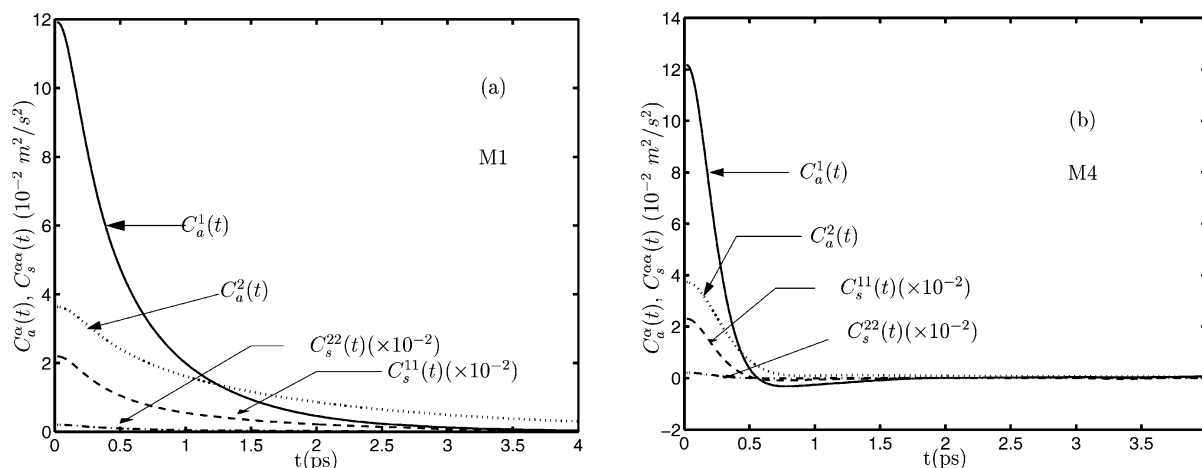


Figure 9. Velocity auto correlation function $C_a^\alpha(t)$ and the correlation between the sum of the velocities $C_s^\alpha(t)$ of each species for (a) M1 and (b) M4. The velocity cross-correlation functions are linear combinations of VACF and the correlations between the sum of the velocities (eq 12).

times, becoming positive after about 3 ps. This trend in the behavior of f_{11} has not been reported in previous bulk mixture studies^{13,21} and was not observed in our recent study of Ar/Kr mixtures in zeolite NaY.²¹ In contrast, the integrals f_{22} and f_{12} remain negative at all times (Figure 8a). In the other three mixtures, M2, M3, and M4, all three running integrals remain negative at all times. In addition, the values of f_{22} and f_{12} have the largest negative values for M1 and get progressively more positive relative to M1 as the ratio σ_{22}/σ_{11} is increased from M1 to M4 (Table 3). It is clear that these trends in $f_{\alpha\beta}$'s dictate the values of \mathcal{D}_d for each of the mixtures investigated. For each mixture f_{11} is seen to possess the largest uncertainties when compared with f_{22} and f_{12} . We attribute this to the lighter mass of species 1. As a result of the relatively small uncertainties seen in f_{22} and f_{12} , the fluctuations in f_{11} are reflected in \mathcal{D}_d (Figure 6).

$f_{\alpha\beta}$'s are the primary quantities needed to calculate the distinct diffusion in the mixture. The dissociation and association in a mixture is due to the inequalities $|f_{11} + f_{22}| < |2f_{12}|$ and $|f_{11} + f_{22}| > |2f_{12}|$, respectively. The values of these inequalities are tabulated in Table 3. To get a deeper insight into reasons for the observed trends in $f_{\alpha\beta}$, the contributions to the cross-correlations based on eq 12 were studied. The cross-correlations between like species, $C_c^{\alpha\alpha}(t)$, is expressed as a linear combination of $C_s^{\alpha\alpha}(t)$, which represents correlations between the momenta of species α , and $C_a^\alpha(t)$, which is simply the VACF of the α th species. Because C_c^{12} cannot be split in a similar manner, eq 12, it is not plotted. Figure 9a,b shows the in-plane components of $C_a^\alpha(t)$ and $C_s^{\alpha\beta}(t)$ of each of the species for mixtures M1 and M4. Note that these data are obtained from a single MD run and, within the relatively small time scale of 4 ps for which the data are presented, fluctuations are virtually absent. We note that the $f_{\alpha\alpha}$'s are obtained as time integrals of the quantities plotted in Figure 9 and the variations of $C_s^{\alpha\alpha}(t)$ and $C_a^\alpha(t)$ at initial times appear to dominate the trends in $f_{\alpha\alpha}$'s (Figure 8). In mixture M1, although the VACF $C_a^1(t)$ has a larger contribution at shorter times, when compared with $C_s^{11}(t)$, the slower relaxation of $C_s^{11}(t)$ leads to a net positive contribution for the time integral f_{11} at longer times. Not only is the value of the VACF for species 2, $C_a^2(t)$, greater at initial times when compared with $C_s^{22}(t)$, but in contrast to component one, the quicker relaxation time and the smaller magnitude of $C_s^{22}(t)$ contribute to an overall negative value for f_{22} . The VACFs for species 1 and 2 for mixture M1 where both species form layers at similar z positions (Figure 4a) are gaslike. For

mixture M4 (Figure 9b) where the individual species have the greatest separation in the z direction, the VACFs are more liquidlike with the small negative regions. In this case the relaxation times for both $C_s^{\alpha\alpha}(t)$ and $C_a^\alpha(t)$ are comparable and the time integrals of $f_{\alpha\alpha}$ are dominated by the differences between the corresponding correlations at short times. This leads to a net negative value for both f_{11} and f_{22} , as shown in Figure 8d.

5.3. Pair Correlation Functions. The in-plane (xy) radial distribution functions plotted in Figure 10 also reveal signatures of dissociative and associative tendencies of the various mixtures. In Figure 10a $g_{\alpha\beta}(r)$ for mixture M1 is plotted. The intensity of $g_{12}(r)$ is less than those of $g_{11}(r)$ and $g_{22}(r)$, suggesting that the probability of locating unlike species in the vicinity of a particle is less than locating like species around it. This is suggestive of a tendency to demix. From mixtures M1 to M4, the $g_{12}(r)$ peak becomes progressively more intense than the corresponding peaks of $g_{11}(r)$ and $g_{22}(r)$, indicative of increased association between unlike species. This feature is clearly observed for mixtures M3 and M4 (Figure 10c,d). The increased association leads to progressively larger negative values of \mathcal{D}_d (Table 2 and Figure 7a). We note that the pair correlation function is not always indicative of an associative tendency²¹ of the mixture as observed here.

The ability of the fluid to form distinct layers as σ_{22}/σ_{11} is increased, appears to dominate the observed trends in \mathcal{D}_d . Although the tendency to separate into distinct layers increases from M1 to M4, as observed in Figure 4 the proximity between the fluid layers is still less than about 0.7 Å (based on the positions of maxima in the layer density distributions), favoring interactions between unlike species. As the pair distributions reveal (Figure 10), the increasing ability of unlike species to interact is enhanced as the species occupy distinct fluid layers in the pore and explains in part the deviation in \mathcal{D}_d from the expected trends in the bulk. When $\sigma_{22}/\sigma_{11} = 1$ (M1), both species compete for the same adsorption sites, hence occupying the same layer within the pore (Figure 4a). In the case of M2, M3, and M4 the unlike particles are not competing for the same region of space. This is evident from the fact that $\rho(z)$ in the case of M2 to M4 (see Figure 4b–d) are at different values of z . Even though this distance is not larger than σ_{12} , the lateral displacement, i.e., displacement within the xy plane ensures that the average distance between particles of type 1 and 2 (see Figure 10b–d) are such that it is the dispersion or attractive

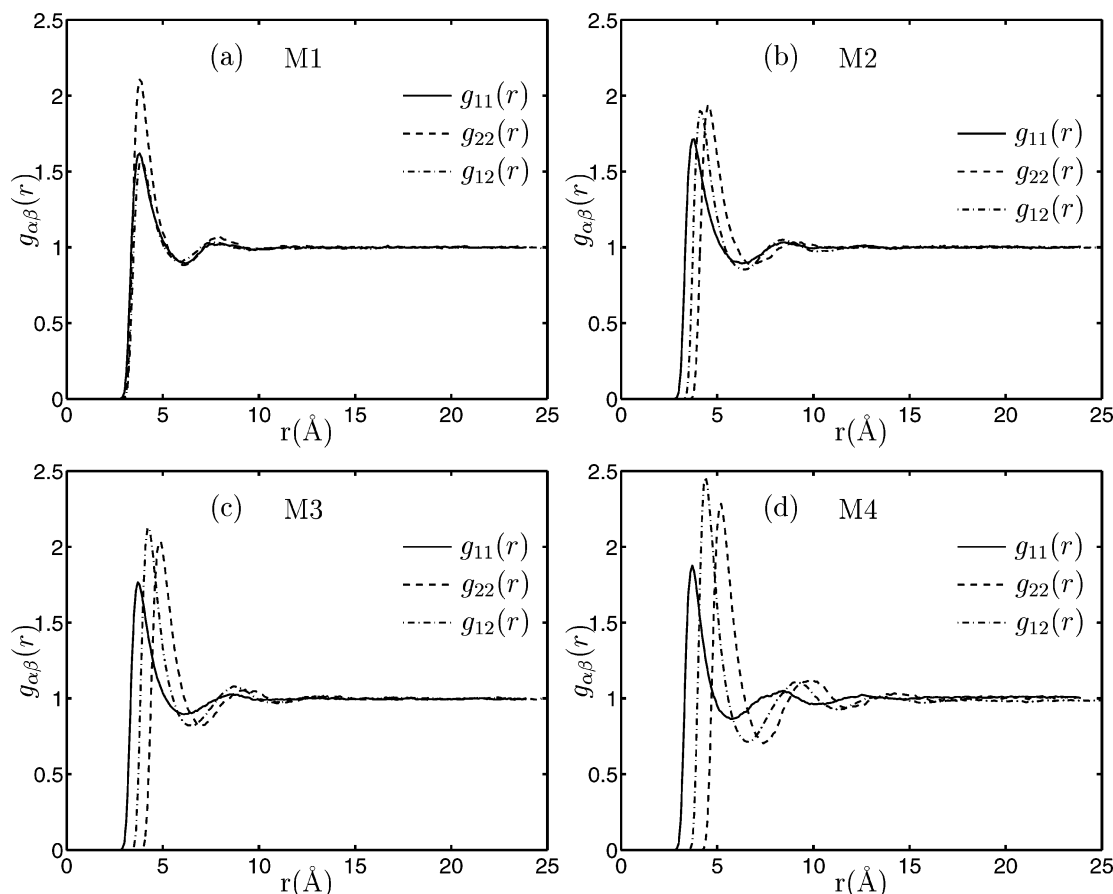


Figure 10. Radial distribution functions in the xy plane (plane parallel to wall). All the three in-plane radial distributions are shown: $g_{11}^{xy}(r)$ (solid), $g_{22}^{xy}(r)$ (dashed), and $g_{12}^{xy}(r)$ (dash-dot) for (a) M1, (b) M2, (c) M3, and (d) M4. The intensity of g_{12} is seen to increase from mixture M1 to M4.

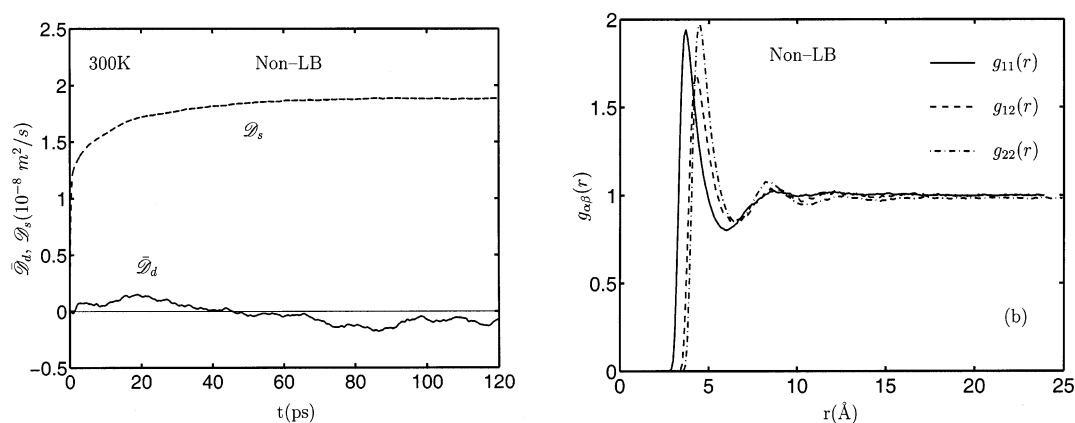


Figure 11. (a) Distinct and mixture self-diffusion coefficients in a non-LB mixture. (b) In-plane radial distribution functions in a non-LB mixture. The potential parameters are similar to mixture M4 with the interaction between unlike species reduced to $\epsilon_{12} = 0.6$ kJ/mol. The intensity of the g_{12} peak is reduced when compared with the corresponding LJ mixture (M4) in Figure 10. The value of $R = 0.949$ for this non-LB mixture indicates increased dissociativity when compared with mixture M4 where $R = 0.833$.

interaction that is predominant. This leads to dynamic association and a value for R that is less than unity.

5.4. Non-LB Mixture. The effect of fluid–fluid attractive interactions between unlike species on the associative tendencies of the mixtures M2–M4 were assessed by computing \mathcal{D}_d for a non-LB mixture. The fluid–fluid interaction between the particles of species one and two, ϵ_{12} , was reduced to 0.6 kJ/mol in mixture M4. This is much smaller than 1.3527 kJ/mol, which is the strength of the interaction parameter in the corresponding LB mixture. All the other parameters were similar to the LB mixture. Figure 11a shows the plot of $\bar{\mathcal{D}}_d$ and \mathcal{D}_s for the non-LB mixture. The $\langle \bar{\mathcal{D}}_d \rangle$ value for this mixture is -0.096

$\times 10^{-8}$ m²/s, $\mathcal{D}_s = 1.879 \times 10^{-8}$ m²/s, and $R = 0.949$. The values indicate that the mixture is not as associative as the corresponding LB mixture M4 where $\langle \bar{\mathcal{D}}_d \rangle = -0.212$ and $R = 0.833$. This confirms the finding of the previous studies on bulk mixtures that, as expected, the fluid–fluid interactions are at least partly responsible for the observed D_d . Additionally, the geometry of the pore also influences the D_d by providing opportunity for the fluid particles to interact, especially when σ_{22}/σ_{11} is increased. This indicates that the pronounced associative nature of the LB mixtures is partly due to the fluid–fluid interactions between unlike species. Figure 11b shows the in-

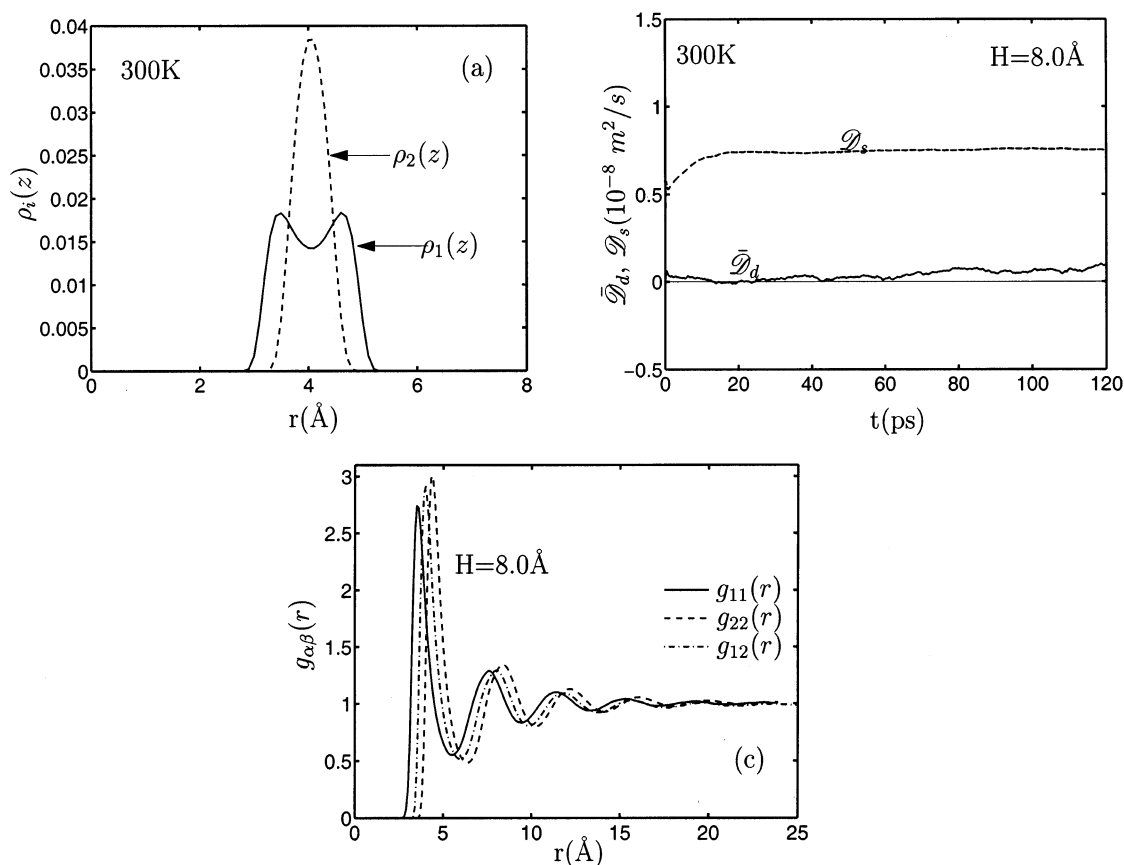


Figure 12. (a) Density distribution, (b) distinct and mixture self-diffusion coefficients, and (c) in-plane radial distribution functions for Ar–Xe in a smaller pore of width $H = 8.0$ Å. Both fluid species form a single layer and occupy central regions of the pore. The value of the ratio $R = 1.08$ for this mixture indicates a weakly dissociative mixture.

plane RDF of the non-LB mixture. Comparing Figures 11b and 10d, the intensity of g_{12} is observed to be stronger in the case of the LB mixture than the corresponding non-LB mixture.

5.5. Influence of Pore Width. In all our simulations, changing the ratio σ_{22}/σ_{11} of the fluid mixture altered the location of fluid layers of unlike species within the pore. Given the geometry of the slit pore this situation will always occur for pore widths at which two fluid layers form. However, simulations at a smaller pore width ($H = 8.0$ Å) was also carried out for the mixture M2 (Ar/Xe mixture), where, although the σ_{22}/σ_{11} ratios differ from unity, both species predominantly occupy the same (central) region of the pore space, as shown in Figure 12a. In this case the distinct diffusion $\langle \bar{\mathcal{D}}_d \rangle = 0.058 \times 10^{-8}$ m²/s, $\bar{\mathcal{D}}_s = 0.754 \times 10^{-8}$ m²/s, and $R = 1.08$. The large value of R is indicative of a dissociative mixture. Hence the benefit of adjacent layering that led to increased interactions between unlike species and a negative value of $\bar{\mathcal{D}}_d$ (associative) for the larger pore width is absent and the mixture is observed to be dissociative, albeit weakly, at the smaller pore width of $H = 8.0$ Å.

6. Conclusion

Mutual diffusion, self-diffusion, and distinct diffusion coefficients for equimolar LJ binary mixtures confined in slit-shaped graphite pores have been computed using molecular dynamics simulations. In all cases the distinct diffusion coefficients are evaluated in a barycentric reference frame. In one of the mixtures (M2) the LJ interaction parameters and atomic masses are similar to that of a Xe–Ar mixture. In the other mixtures (M1, M3, and M4) only the size ratios were varied, keeping all other parameters being similar to those for mixture M1. Our study

reveals that the location of the layers of the different species in the slit pore strongly influences the character of the distinct diffusion. Excepting one case, all studies were carried out at pore widths at which two fluid layers are adsorbed in the pore. When both species occupy the same layer in the pore (M1) the distinct diffusion is found to be positive. As the size ratio is increased and both species occupy different layers, the distinct diffusion is found to become progressively more negative. This increased association in the mixtures as the size ratio is increased is contrary to the expected trend in the bulk where the mixtures should become increasingly dissociative. Our study indicates that this deviation from bulk behavior is due to the formation of distinct fluid layers, giving unlike species a greater opportunity to interact than they would in the bulk. In-plane pair correlation functions also reveal the increased association between unlike species as the size ratio is increased. Our study additionally reveals that the pore width can also alter the distinct diffusion. The Ar–Xe mixture (M2) is associative with negative values of the distinct diffusion when the fluid forms two layers in the pore. However, at smaller pore widths, where only a single layer is accommodated, the mixture is observed to be dissociative.

References and Notes

- (1) Gergidis, L. N.; Theodorou, D. N. *J. Phys. Chem. B* **1999**, *103*, 3380.
- (2) Snurr, R. Q.; Kärger, J. *J. Phys. Chem. B* **1997**, *101*, 6469.
- (3) Jost, S.; Fritzsche, S.; Haberlandt, R. *Chem. Phys. Lett.* **1997**, *279*, 385.
- (4) Schuring, D.; Koriabkina, A. O.; de Jong, A. M.; Smit, B.; van Santen, R. A. *J. Phys. Chem. B* **2001**, *105*, 7690.
- (5) Ayappa, K. G. *Langmuir* **1998**, *14*, 880.

- (6) Cracknell, R. F.; Nicholson, D.; Quirke, N. *Mol. Phys.* **1993**, *80*, 885.
- (7) Curry, J. E.; Cushman, J. H. *Mol. Phys.* **1995**, *85*, 173.
- (8) Somers, S. A.; McCormick, A. V.; Davis, H. T. *J. Chem. Phys.* **1993**, *99*, 9890.
- (9) Shevade, Abhijit V.; Jiang, S.; Gubbins, K. E. *J. Chem. Phys.* **2000**, *113*, 6933.
- (10) Israelachvili, J. *Intermolecular and Surface Forces: with Applications to Colloidal and Biological Systems*; Academic: London, 1985.
- (11) Somers, S. A.; Ayappa, K. G.; McCormick, A. V.; Davis, H. T. *Adsorption* **1996**, *2*, 33.
- (12) Zwanzig, R. *Annu. Rev. Phys. Chem.* **1965**, *16*, 67.
- (13) Zhou, Y.; Miller, G. H. *Phys. Rev. E* **1996**, *53*, 1587–1601.
- (14) van den Berg, H. P.; Hoheisel, C. *Phys. Rev. A* **1990**, *42*, 2090–2095.
- (15) Schoen, M.; Hoheisel, C. *Mol. Phys.* **1984**, *52*, 33–56.
- (16) Schoen, M.; Hoheisel, C. *Mol. Phys.* **1984**, *52*, 1029–1042.
- (17) van den berg, H. P.; Hoheisel, C. *Phys. Rev. A* **1990**, *42*, 3368–3373.
- (18) Trullas, J.; Padro, J. A. *Phys. Rev. E* **1994**, *50*, 1162–1170.
- (19) Hansen, J. P.; McDonald, I. R. *Phys. Rev. A* **1975**, *11*, 2111.
- (20) Sanborn, M. J.; Snurr, R. Q. *Sep. Purif. Technol.* **2000**, *20*, 1–13.
- (21) Kamala, C. R.; Ayappa, K. G.; Yashonath, S. *Phys. Rev. E* **2002**, *65*, 061202.
- (22) Thompson, A. P.; Heffelfinger, G. S. *J. Chem. Phys.* **1999**, *110*, 10693.
- (23) Xu, L.; Tsotsis, T. T.; Sahimi, M. *J. Chem. Phys.* **1999**, *111*, 3252.
- (24) Cracknell, R. F.; Nicholson, D.; Quirke, N. *Phys. Rev. Lett.* **1995**, *74*, 2463.
- (25) de Groot, S. R.; Mazur, P. *Non-Equilibrium Thermodynamics*; Dover Publications, Inc.: New York, 1984.
- (26) Hansen, J. P.; McDonald, I. R. *Theory of Simple Liquids*; Academic-Press: London, 1976.
- (27) Steele, W. A. *Surf. Sci.* **1973**, *36*, 317.
- (28) Allen, M. P.; Tildesley, D. J. *Computer Simulation of Liquids*; Clarendon-Press: Oxford, 1987.
- (29) Powles, J. G.; Dornford-smith, A.; Evans, W. A. B. *Phys. Rev. Lett.* **1991**, *66*, 1177.